High resolution structures of Myosin-IC reveal a unique actin-binding orientation, ADP release pathway, and power stroke trajectory

Sai Shashank Chavali[1#], Peter J. Carman[2,3,4], Henry Shuman[3,4], E. Michael Ostap[3,4,5*] and Charles V. Sindelar[1*†]

[1]Department of Molecular Biophysics and Biochemistry
Yale University, PO Box 208103, New Haven, CT 06520-8103 USA

[2]Biochemistry and Molecular Biophysics Graduate Group, Perelman School of Medicine, University of Pennsylvania; Philadelphia, Pennsylvania, USA

[3]Pennsylvania Muscle Institute, Perelman School of Medicine at the University of Pennsylvania, Philadelphia, PA 19104;

[4]Department of Physiology, Perelman School of Medicine at the University of Pennsylvania, Philadelphia, PA 19104

[5]Center for Engineering Mechanobiology, Perelman School of Medicine at the University of Pennsylvania, Philadelphia, PA 19104

[#]Current address: Treeline Biosciences, Watertown, MA
[†]Current address: New Haven, CT

*Correspondence: Address correspondence to ostap@pennmedicine.upenn.edu or sindelar@alum.mit.edu

Competing Interests Statement: The authors declare no competing interest.

31 **Significance Statement**

32 Myosin-IC (myo1c) uses an ATP-driven 'power-stroke' to support slow intracellular membrane
33 and vesicle transport. We used cryo-electron microscopy to understand adaptations of myo1c to
34 perform its unique roles. We discovered an altered interface between myo1c and actin
35 compared with the closely related myo1b, which repositions the motor domain and alters the
36 trajectory of its lever arm swing compared to other myosins. This explains why myo1c propels
37 actin filaments in a leftward circular path. We also discovered a unique role in force sensing for
38 a structural element called the N-terminal extension and built a full-length atomic model for the
39 myo1c power-stroke. Our findings highlight how myosins can tune their power-stroke
40 geometries and force-sensing properties to adapt to diverse cellular functions.

Abstract

Myosin-IC (myo1c) is a class-I myosin that supports transport and remodeling of the plasma membrane and membrane-bound vesicles. Like other members of the myosin family, its biochemical kinetics are altered in response to changes in mechanical loads that resist the power stroke. However, myo1c is unique in that the primary force-sensitive kinetic transition is the isomerization that follows ATP binding, not ADP release as in other slow myosins. Myo1c also powers actin gliding along curved paths, propelling actin filaments in leftward circles. To understand the origins of this unique force-sensing and motile behavior, we solved actin-bound myo1c cryo-EM structures in the presence and absence of ADP. Our structures reveal that in contrast with other myosins, the myo1c lever arm swing is skewed, partly due to a different actin interface that reorients the motor domain on actin. The structures also reveal unique nucleotide-dependent behavior of both the nucleotide pocket as well as an element called the N-terminal extension. We incorporate these observations into a model that explains why force primarily regulates ATP binding in myo1c, rather than ADP release as in other myosins. Integrating our cryo-EM data with available crystallography structures allows the modeling of full-length myo1c during force generation, supplying insights into its role in membrane remodeling. These results highlight how relatively minor sequence differences in members of the myosin superfamily can significantly alter power stroke geometry and force-sensing properties, with important implications for biological function.

63 **Introduction**

64 Members of the myosin family of cytoskeletal motors function in a wide range of cell
65 processes that include muscle contraction, organelle transport, cell adhesion, signal
66 transduction, and cell division. The motor domain of each myosin paralog evolved
67 mechanochemical properties suited to carry out these diverse functions (1, 2). Notably, the
68 ATPase activities and motility rates of myosin paralogs can differ by three orders of magnitude
69 (2, 3), with strikingly different sensitivities to mechanical load resulting in motors with varied
70 force-velocity relationships and power outputs (1). Determining how sequences within the
71 highly conserved motor domains lead to such diverse mechanochemistry has been a challenge
72 to the field.

73 Myosin-Is are a family of single-headed, membrane-associated motors that function in
74 cellular processes related to membrane morphology and trafficking, tension sensing, regulation
75 of actin dynamics, and nuclear transcription (4, 5). Like the myosin superfamily overall, there is
76 substantial mechanochemical diversity within the myosin-I family (5). For example, two widely
77 expressed vertebrate paralogs, myo1b and myo1c, have similar slow biochemical kinetics (6-9).
78 However, optical trapping studies show that the actin detachment rate of myo1b is slowed
79 ~100-fold by mechanical loads < 2 pN (10, 11), while myo1c is relatively insensitive to loads in
80 this range (8). This dissimilarity is due to differences in the sensitivity of ADP release to
81 mechanical loads. Functionally, myo1b has mechanochemistry suited to force-sensitive actin
82 anchoring, while myo1c is suited to generating power under loads (1). An additional interesting
83 difference is that myo1c is able to turn actin filaments in leftward circles in gliding assays (12),
84 which is a property that may be related to establishment of cell chirality (13).

85 In previous work, we determined the high-resolution structures of rigor and ADP-bound,
86 tension-sensitive states of actin-bound myo1b from rat (14). Biophysical studies based on
87 these structures revealed a role for the N-terminus of the protein in communicating the
88 presence of mechanical loads to the nucleotide binding site, which affect ADP release (14-16).
89 We termed this region the N-terminal extension (NTE) and showed that it interacts with the N-
90 terminal subdomain of the motor, the lever arm helix, and the converter domain. Its sequence
91 is variable among myosin-Is, and similar regions exist in other myosin paralogs (16-18);
92 however, it is not present in myosin-V (19). Although the importance of the NTE has been
93 established for modulating the rate of ADP release (15, 16), it is not clear how sequence
94 differences in the motor lead to altered force sensitivity.
95 The ability of myosins to adjust their kinetic properties in response to force is important
96 for tuning force-velocity relationships in muscle (20-23), facilitating processive stepping of
97 transport motors (24), and maintaining tension of membranes (10). Interestingly, the
98 biochemical step of myo1c that is most sensitive to mechanical loads is different from other
99 myosins that have been studied, including myo1b, myo5, myo6, smooth muscle myosin
100 (MYH11), and cardiac muscle myosin (MYH7). While other characterized myosins respond to
101 force by slowing ADP release, myo1c responds by slowing the isomerization that follows ATP
102 binding (8). The origin of this fundamental difference in behavior of myo1c has remained
103 obscure. In part, this is because the structural origins of ADP force-sensitivity also remain
104 incompletely understood.
105 In this work, we report the high-resolution structures of the ADP-bound and rigor (AM)
106 states of actin-bound myo1c (actomyo1c) expressed without its membrane-binding tail domain

107 (residues 1-767; see Methods) and we compare the structures to actin-bound myo1b. We
108 discovered that myo1c binds to actin in a unique orientation that produces a 'skewed' power
109 stroke with respect to the actin filament, and that this effect is enhanced by an inherent skew
110 of the myo1c power stroke itself, compared with myo1b. The skewed power stroke may explain
111 the motor's ability to turn actin filaments in gliding assays (12). Moreover, we find differences
112 from myo1b in the structural relationship between the nucleotide binding site and position of
113 the lever arm helix that provide a rationale for differences in force sensitivity. Finally, our new
114 structures allow us to model the full working stroke of the full length myo1c molecule,
115 providing insights into function of the native molecule. These results provide for a more
116 complete understanding of the coupling of the ATPase cycle and lever arm position of myosins.
117

118 **Results**

119 **Two-step isomerization visualized during the myo1c ADP lever arm swing**

120 We generated complexes of a mouse myo1c construct containing three IQ motifs and
121 calmodulin bound to actin filaments and solved atomic-resolution structures both in the
122 absence and presence of 1 mM MgADP (Fig. 1). The resolution of the myo1c motor domain
123 (Fourier shell correlation, 0.143) was estimated as 2.7 Å for the rigor state (AM) and 2.8 Å for
124 the ADP-bound state (AM.ADP; Fig. S1). This resolution allowed modeling of the protein chains
125 throughout the actin, motor, and first IQ motif (Fig. 1). The resolutions of the lever arm helix
126 and calmodulins beyond the first IQ motif were substantially lower than those above, so we did
127 not include these regions in the final structures.

128 The structures reveal a tilting of the lever arm going from a principal ADP-bound state
129 conformation ($AM.ADP^A$) to the AM state (Fig. 1; Fig. S2 - S4) as seen previously at low
130 resolution (9). Similar to what was observed for actin-bound myo1b, but unlike other myosins
131 that have been studied (14), 3D classification revealed a second ADP-bound population
132 ($AM.ADP^B$) whose lever arm has repositioned to a rigor-like orientation (Fig. 1B; Fig. S3).
133 Classification analysis indicates this $AM.ADP^B$ population may comprise ~5% of the total
134 particles (Fig. S4). The myo1c lever tilts 24° from $AM.ADP^A$ to $AM.ADP^B$ and < 2° from $AM.ADP^B$
135 to AM (Fig. 1). Corresponding myo1b lever arm rotations were 25° and 5°, respectively (14);
136 thus, we propose that, similar to myo1b, the three myo1c conformational states give a
137 mechanistic succession of states proceeding from $AM.ADP^A$ to $AM.ADP^B$ to AM (14).

138 Despite these similarities, however, myo1c $AM.ADP^B$ and AM conformations are not the
139 same as in myo1b. In myo1c, conformational changes within the motor domain that accompany

140 ADP release appear largely complete in the AM.ADP^{B} structure, and the AM structure differs
141 little from AM.ADP^{B} (0.7 Å backbone RMSD; Table S1). In contrast, the myo1b nucleotide cleft
142 opens only partially in AM.ADP^{B}, and further opening of the nucleotide cleft with ADP release
143 results in an AM conformation distinct from AM.ADP^{B} (1.2 Å RMSD; Table S2). As shown below,
144 differing behavior of the myo1c and myo1b motor domains during ADP release is linked
145 to significant functional differences that are observed between these two motors.
146
147 **An off-axis myo1c ADP lever arm swing**
148 Cryo-EM models reveal that the actin-bound myo1c lever arm swing upon ADP release is
149 skewed 32° from the long axis of the actin filament, while the myo1b ADP lever arm swing is
150 much more parallel (7° skew) (Fig. 2). When modeled in the context of an actin gliding assay,
151 skewing of the myo1c ADP swing is predicted to push the leading tip of an actin filament to the
152 left (Fig. S5-S7). These observations provide a plausible mechanism by which myo1c promotes
153 left-handed circular, rather than straight, gliding of actin filaments in *in vitro* motility assays (12,
154 13).
155 More detailed comparison of the myo1c and myo1b ADP lever arm swings reveals two
156 distinct factors that both contribute to the off-axis lever arm swing in myo1c: the binding
157 orientation of the motor domain on actin, and changes in the lever arm swing geometry
158 inherent to the motor domain itself. The binding orientation, or perch, of the myo1c motor on
159 actin is different from myo1b (Fig. 2A–B). The myo1c perch is defined by distinctive interactions
160 at the actin-binding interface (Fig. 2; Movie S2; see below). The myo1c actin-binding region in
161 our structures (upper- and lower-50 kDa domains) remain mostly static in our structures,

162 evidenced by minimal movements of the two domains relative to each other (no more than 1–
163 3° rotation; see Fig. 3A-B). The lower 50-kDa domain can therefore be used as a measure of the
164 motor orientation change with respect to actin.

165 In our myo1c structures the actin-binding region rotates 6–8° counterclockwise
166 compared to myo1b when looking down on the motor perpendicular to the filament axis (Fig.
167 2B; Movie S1). This orientation change redirects the ADP lever arm swing of myo1c, making it
168 ~4° less parallel to the filament long axis than if it assumed the myo1b perch orientation (Fig.
169 S7B and Movie S1, compare green to pink cylinders; see also Fig. S7C). We expect the myo1c
170 primary lever arm swing from the pre-power stroke state represented by (PDB:4BYF) to
171 AM.ADP^{A} would be similarly affected. Strikingly, while perch differences are evident in other
172 reported actomyosin structures, the motor domains tend to reorient in a manner that would
173 not be expected to skew the lever arm swing significantly compared with myo1b (Fig. S8). We
174 note that a low-resolution structure of *Acanthamoeba* myosin-IB was also reported to have a
175 unique binding orientation on actin (25), but it remains unclear what affect this would have on
176 the lever arm swing trajectory.

177 Skew of the myo1c AM lever arm swing caused by the unique perch orientation is
178 greatly enhanced by unique lever arm geometries inherent to the motor domain itself. We
179 quantified this effect by computing the lever arm rotation axis that would result if the myo1c
180 motor domain assumed the same perch orientation on actin as myo1b (Fig. S7B and Movie S1,
181 green cylinders). The resulting skew of this 'myo1b-oriented' myo1c ADP lever swing, 28°, is
182 much larger that of the myo1b ADP lever swing (7°) (Fig. S7B and Movie S1, white cylinders).

183 The total myo1c ADP lever swing skew (32°; Fig. S7B, pink cylinders) is even larger due to the 4°
184 perch difference.

185 Comparing lever arm orientations when motor domains are aligned reveals that the
186 skewed myo1c lever swing is mainly due to a difference with the AM lever arm position. Lever
187 orientations of aligned myo1b and myo1c AM.ADP^{A} motor domains are within ~2–3° of one
188 another (Fig. S7C, compare middle black and green data points; Tables S5–S6). However, lever
189 orientations of aligned AM structures differ more substantially between the two isoforms,
190 resulting in a significant off-axis component (azimuthal angle change) of the ADP lever arm
191 swing for myo1c but not myo1b (11° and 3°, respectively; Fig. S7C, right side and Tables S5–S6).
192 This inherent difference between myo1b and myo1c AM lever arm positions may originate from
193 different structural environments of the lever in this state; in particular, in myo1b loop-5
194 maintains contact with the lever in all three structural states (AM.ADP^{A} , AM.ADP^{B} and AM),
195 while this contact is lost in the myo1c AM.ADP^{B} and AM structures (Movie S1; also see below).
196 In summary, compared with myo1b, myo1c skews its ADP swing off-axis by concomitantly
197 changing its perch on actin and adjusting the AM lever position.

198

199 **Structural determinants of the myo1c perch orientation on actin**

200 The cryo-EM density of the myo1c actin-binding site reveals well-defined side chains and
201 other features consistent with the reported resolution of 2.7 - 3.0 Å (Fig. S2) and is essentially
202 indistinguishable in the AM.ADP^{A}, AM.ADP^{B}, and AM states. Thus, we used the highest
203 resolution structure (AM) to identify changes at the myo1c actin binding site compared with
204 myo1b that drive reorientation of the perch (Fig. 2B-E; Movie S2). Overall, myo1c actin-binding

205 loops on the periphery of the interface principally drive the reorientation, as was observed in
206 structural studies of PfMyoA (26).

207 Sequence and structure differences at three distinct sites of the myo1c actin interface
208 drive the unique orientation: Loop-2 (K553 – T564) in the upper 50-kDa domain, and loop-3
209 (T490 – E506) and the activation loop (E450–G454) in the lower 50-kDa domain. Reorientation
210 occurs about a fixed pivot point on actin, where conserved P466 in the lower 50-kDa domain
211 rests in a hydrophobic pocket (Fig. 2D, E). Notably, the cardiomyopathy loop and loop-4 have
212 unique structures, but are positioned similarly to other characterized myosins (27).

213 Loop-2 (K553 - T564) connects the upper and lower 50-kDa domains while interacting
214 with actin where it plays a role in reorienting myo1c on actin. While loop-2 is largely disordered
215 in the Myo1c.ADP.VO_4 (PDB: 4BYF; (28)) crystal structure, it is well ordered and resolved in the
216 three actomyo1c states. The loop-2 C-terminus is fixed on actin near the P466 pivot in both
217 myo1c and myo1b, supported by hydrogen bonds of R561 with actin S344 and S348 (Fig. S6C,
218 D). However, a helix-loop-helix motif immediately N-terminal to loop-2 operates as a spacer
219 that lengthens the loop by ~2.5 Å in myo1c, holding the upper 50 kDa domain farther away
220 from the actin surface than myo1b (Fig. S6C; Movie S2). A major determinant of the spacer
221 restructuring in myo1c is the loss of two prolines from the myo1b spacer sequence (myo1b
222 P555, P559). These sites surround a glutamic acid (myo1b E556; myo1c E555) that makes a
223 conserved salt bridge with an arginine (myo1b R359; myo1c R353) in a neighboring α-helix of
224 the upper 50-kDa domain. These differences and other sequence changes, including D552,
225 K553, and S554 in myo1c that orients and stabilizes an α-helical turn S555-S558) drive the
226 spacer lengthening. The spacer function we identify for loop-2 in myo1b and myo1c may be

227 related to another posited role of loop-2, which is to mediate the initial interaction between
228 some myosins and actin (27, 29), thereby regulating actin-activated ATPase activity.
229 Loop-3 (T490-E506) in the lower 50-kDa domain is the other major actin interface that
230 accommodates the myo1c binding reorientation. Myo1c loop-3 shifts ~2 Å away from the actin
231 surface compared with myo1b and other myosins (Fig. 2C; Fig. S6A; Movie S2). Substitution of
232 extended hydrophilic side chains (Q496, R499, K500 and R504) in place of shorter counterparts
233 in myo1b (N496, D502, T503 and H507, respectively) supports this shift, as well as restructuring
234 of the actin-proximal part of this loop into an α-helical turn to shift R499 and K500 backbone
235 positions closer to the actin surface in myo1c (Fig. 2C; Fig. S6A). When myo1c binds to actin,
236 actin Y91 is flipped 120° compared to when myo1b binds. This reorientation allows Y91 to fill a
237 vacant space in the myo1c structure that would otherwise be occupied by the more closely
238 positioned loop-3 of myo1b. As a result, despite being farther away from actin than in myo1b,
239 myo1c loop-3 maintains a similar number of actin contacts, with both electrostatic and
240 hydrophobic character. Interestingly, the actin-detached myo1c.ADP.VO4 structure (PDB: 4BYF;
241 (28)) shows a similar loop conformation to the cryo-EM structures, suggesting that the loop's
242 shape is maintained by its internal structure.
243 The myo1c activation loop (E450-G454) is also shifted on the actin surface compared
244 with myo1b (Fig. 2D). The activation loop is a short region between the HQ and HR helices in
245 the lower 50-kDa region of myosin (30). Upon actin binding, it is thought to accelerate the
246 movement of the relay helix, which stimulates ATPase activity (31). F452 of myo1c forms a
247 hydrophobic interaction with Q353 and a possible backbone interaction with S350 of actin. In
248 contrast, the residue corresponding to F452 in the myo1b activation loop (T448) does not

249 interact with actin, and other actin interactions of the loop are minimal, limited to a single
250 backbone hydrogen bond of N447 with actin S350 (Fig. S6B). Although not resolved, K453 likely
251 interacts with the N-terminal acidic residues (E4) of actin.

252 The cardiomyopathy loop (T319-P333) in the upper 50-kDa region also plays a significant
253 role in the myo1c binding orientation change. However, unlike loop-3 and the activation loop,
254 the cardiomyopathy loop is positioned similarly on actin as other characterized myosins (27)
255 and maintains a similar (although not identical) structure. Instead, to compensate for the
256 different motor domain orientation of myo1c, the cardiomyopathy loop swivels ~5° on the
257 upper 50-kDa subdomain compared with myo1b. The new cardiomyopathy loop orientation
258 relative to the motor is supported by orientation changes of the short helices at the base of
259 loop-2 due to hydrophobic repacking. In particular the short helix in myo1c 535-539 is shifted
260 such that it follows the cardiomyopathy orientation change. The cardiomyopathy loop contains
261 residues that form hydrophobic interactions observed in other myosins (I323, A325, L330). The
262 side chains of S332 and R321 of myosin form a unique charge cluster with side chain of E334 of
263 actin, and E328 of myo1c interacts with K336 and Y337 of actin. The K336 and Y337
264 interactions are intriguing, because these residues are involved in the "flattening" of the actin
265 subunit as it polymerizes to form F-actin. Given the proposal that some myosins affect actin
266 nucleation and polymerization (32), the effect of this interaction on actin dynamics should be
267 explored.

268 Other actin-interacting regions of myo1c contribute less to the binding orientation
269 change. The helix-loop-helix motif adjacent to loop-3 is situated very close to the binding
270 orientation pivot axis (not shown), so that actin interactions are very similar to other myosins,

271 and the interacting residues are more conserved. The helix-loop-helix motif stabilizes the DNase
272 binding loop (D-loop) of actin, as found for other myosins (27). This includes the side chain of
273 myosin's E476 with K50 of actin. There is a complex network of interactions that both stabilize
274 the helix-loop-helix structure and interact with two adjacent actin subunits, including E461,
275 E462, and K477 of myosin with T351 and G46 of actin. L472, L475, and L478 of myosin form a
276 hydrophobic patch that positions loop-3.

277 Loop-4 (N281-E297) in the upper 50-kDa subdomain is differently composed than in
278 myo1b and is located farther from the actin surface. In contrast to hydrophobic actin contacts
279 made by myo1b loop-4, E288 backbone and D289 side chain atoms from myo1c loop-4 possibly
280 interact electrostatically with K328 of actin; however, these residues are poorly resolved. The
281 sequence and orientation of this loop likely explain the competition between myo1c and
282 tropomyosin for binding to actin, as shown in *in vitro* motility and biochemical experiments (33,
283 34).

284

285 **Opening of the active site accommodates ADP release**

286 The overall behavior of myo1c during ADP release, as captured by our structures,
287 generally parallels myo1b; however, differences in the details correlate with highly significant
288 functional differences between the two motors. Both motors make a large-angle lever swing
289 (~25°) during ADP release (9, 35), accompanied by a significant rotation (~10°) of the N-terminal
290 domain to open the nucleotide pocket, and both motors dock their NTE segments into a cavity
291 between the motor domain and the lever in the AM conformation. Moreover, both motors
292 exhibit small sub-populations of the ADP state (AM.ADP^{B}) where the lever has swung to an

293 angle that approaches the AM position. This behavior differs from other myosins, where
294 multiple ADP conformations have not been reported. However, details of nucleotide pocket
295 opening and its coordination with NTE docking and lever arm tilting during ADP release differ
296 substantially between myo1c and myo1b. These structural relationships are likely crucial for
297 setting force sensitivity.

298 The global conformational changes in myo1c that accompany active site opening during
299 ADP release are largely completed in the AM.ADP^{B} state. Subdomain motions of the three
300 states can be described by approximate rigid body rotation of the converter/lever arm helix and
301 the N-terminal subdomain (G12-R97 and K592-G626) in relation to the remainder of the motor
302 domain. The myo1c AM.ADP^{A} to AM.ADP^{B} transition is accompanied by a 10° rotation of the N-
303 terminal subdomain against the upper 50-kDa subdomain, reflecting opening of the active site;
304 very little rotation of the subdomains is then observed in the AM.ADP^{B} to AM transition (< 1°).
305 A related observation is that, while density corresponding to Mg^{2+} is pronounced in the myo1c
306 AM.ADP^{A} nucleotide pocket (Fig. S3A), it is weak or absent in the AM.ADP^{B} structure (Fig. S3B),
307 presumably because the nucleotide pocket opens to a rigor-like conformation that disrupts the
308 Mg^{2+} binding site (19). In contrast, the rotations of the myo1b N-terminal subdomain are
309 equally divided between the AM.ADP^{A} to AM.ADP^{B} transition (5°) and the AM.ADP^{B} to AM
310 transition (5°), reflecting incremental openings of the active site that occur in each step (see
311 also Table S2). Reflecting this difference, Mg^{2+} evidently remains able to bind in myo1b
312 AM.ADP^{B}, prior to the cleft opening more fully in AM to release Mg^{2+} and the nucleotide (14).

313 The opening of the myo1c active site during ADP release occurs through the movement
314 of the HF helix away from the HH helix, increasing the distance between switch-1 and the P-

315 loop (Fig. 3). At their ends where HF and HH are connected by loop-1 (T125 - A128), these
316 helices in myo1c remain closer to each other than seen in myo1b. The other ends of the helices
317 make a minor “chopstick” movement going from AM.ADP^{A} to AM.ADP^{B}, such that the P-loop
318 and switch-1 loop translate away from each other by ~1.2 Å. This movement is very different
319 from the movement of the HF helix observed in myo1b and myo5 (14, 36), where there is a
320 significant axial helix-helix sliding component.

321 During the transition from AM.ADP^{A} to AM.ADP^{B}, the P-loop and the C-terminally
322 connected HF helix move laterally ~2 Å away from switch-1 and its N-terminally connected HH
323 helix. During this transition, hydrogen bonds are formed between N157 in switch-1 and S107 in
324 the P-loop. Despite high conservation of these residues, this interaction was not seen in myo1b
325 or myo5, but was reported in myo15 (14, 32, 36). It is notable that this P-loop switch-1
326 interaction combines with a highly conserved H-bond between neighboring G108 of the P-loop
327 and N53 of the A-loop (S51 - R63; (36)) in the N-terminal subdomain, making an H-bond
328 interaction "belt” in AM.ADP^{B} that holds the active site in a conformation permissible for
329 nucleotide release and binding (Fig. 3E).

330 The conformational transition from myo1c AM.ADP^{B} to AM is subtle compared with
331 myo1b. This is likely due to the P-loop to switch-1 H-bond constraining the P-loop movement.
332 As a result, the HF helix/P-loop element fails to make a 'piston-like' axial movement away from
333 switch-2 seen in the corresponding myo1b transition (14). However, the myo1c transition from
334 AM.ADP^{B} to AM features a 'breathing' movement of the upper 50 kDa domain and N-terminal
335 subdomains (Fig. 3B-C, Fig. S9, Movie S2) accompanied by perturbation of the H-bond between
336 the P-loop and N53 (2.9 to 3.6 Å; Fig. 3D, E). This 'breathing' movement thus correlates with

337 opening of the AM active site in a manner that would likely be less amenable to strong
338 nucleotide binding.
339
340 **Y75 and E76 in loop-5 have key roles in the transition of the lever from AM.ADP^{A} to AM.ADP^{B}**
341 Similar to the changes in the active site, tilting of the myo1c lever and accompanying
342 movements in the N-terminal subdomain are largely complete in the transition from AM.ADP^{A}
343 to AM.ADP^{B}. There is little change in the positions of the lever, NTE, and N-terminal subdomain
344 in the subsequent transition to AM (Fig.'s 1, 3; Movie S3).
345 Two critical residues (Y75, E76) in loop-5 (R70 - H80) are involved in the transition of the
346 lever from myo1c AM.ADP^{A} to the conformation seen in AM.ADP^{B} and AM (Fig. 4). In the
347 AM.ADP^{A} state these residues form a bridge between the motor domain and the lever (Fig. 4C-
348 E). Y75 in loop-5 is found in a hydrophobic pocket with L688 and F689 of the converter, which
349 we term the 'L5–lever bridge,' while E76 forms a cluster of interactions with residues in the
350 converter and lever arm (R639, Y640, E692).
351 Rotation of the N-terminal subdomain from AM.ADP^{A} to the AM.ADP^{B}/AM states
352 concomitantly opens the nucleotide cleft and moves L5 away from the lever. This movement
353 disrupts the L5–lever bridge by pulling Y75 out of the converter hydrophobic pocket and
354 breaking a cluster of interactions between E76 and the lever (Fig. 4C–D). Disruption of this
355 bridge allows the lever to tilt, completing the ADP swing. While L5 is evidently more mobile in
356 our AM.ADP^{B}/AM cryo-EM maps and density for these side chains is weak or absent, modeling
357 indicates that Y75 repacks with neighboring F74 in loop-5, and E76 forms a new cluster of

358 interactions with the converter (Y629 and R631) and the docked NTE (E2, see below),
359 supporting the AM.ADP^B/AM lever position (Fig. 4E).
360 The equivalent of Y75 is conserved in myo1b (Y78) but does not interact with the
361 neighboring F74 (F77) in AM.ADP^B or AM. Rather, it adopts a different rotamer that maintains
362 hydrophobic contact with the lever following the ADP lever arm swing, and blocks the lever
363 from tilting back. Thus, in contrast to myo1c, the L5–lever bridge in myo1b does not break as
364 the lever swings during the transition to AM.ADP^B and AM states. Instead, the bridge stretches
365 and maintains contact with the lever by swiveling the aromatic residue pair (F77, Y78) away
366 from each other in AM.ADP^B and AM conformations (Fig. 4G).
367 The differing behavior of the L5–lever bridge in the two motors is supported by side
368 chain substitutions in myo1c that alter motor domain contacts made by the conserved
369 phenylalanine. In myo1b the F77 side chain conformation is kept in a similar conformation
370 throughout ADP release by hydrophobic contacts with an adjacent helix (side chains L87 and
371 E90). E90 also sterically blocks F77 from pivoting towards Y78 (Fig. 4F-G). In myo1c, L87 and E90
372 are replaced by smaller side chains (V84 and T87) that are too short to contact F77, thus
373 enabling F77 to pivot towards Y78 in the AM.ADP^B and AM conformations, breaking the
374 hydrophobic bridge as ADP is released (Fig. 4D-E). Additionally, the E2 interaction cluster (Fig.
375 4D) is not observed in myo1b, as the myo1b NTE blocks the ability of E76 (E79 in myo1b) to
376 interact with the conserved residues in the converter. The L5–lever bridge appears to be a
377 critical determinant of force-sensitivity; in particular, failure of myo1c to maintain this bridge
378 throughout the ADP lever arm swing likely disables ADP force-sensitivity (see Discussion).
379

380 **Myo1c NTE has a unique structure that stabilizes the lever arm position**

381 The NTE is a crucial participant in the AM.ADP to AM transition, as it markedly
382 accelerates the rate of ADP release and mechanically stabilizes the AM state under load (15,
383 16). Accompanying the opening of the active site and tilting of the N-terminal subdomain in the
384 AM.ADP^{A} to AM.ADP^{B} transition, we observe NTE docking in a pocket formed by the N-terminal
385 subdomain, converter, and lever arm (Fig. 4).

386 The docked NTE locks the myo1c lever into place in AM.ADP^{B} and AM through a network
387 of interactions that are dominated by cation-pi, salt bridge, and H-bond interactions. R8 has a
388 prominent role in this network that we call an 'arginine lock,' forming an apparent cation-pi
389 bond with F689, and simultaneously forming a salt bridge with D693 to stabilize the lever arm
390 position (Fig. 4B). R8 also forms a backbone hydrogen bond interaction with L5 of the NTE. The
391 arginine-lock is not present in myo1b, where NTE docking is dominated by hydrophobic
392 interactions. M1 of the docked myo1c NTE makes hydrophobic contacts with V77 and P78 of
393 loop-5.

394

395 **Deletion of the myo1c NTE disrupts the AM lever position and alters the nucleotide pocket**

396 Deleting the myo1c N-terminus (E2-V10; myo1c$^{\Delta N}$) substantially slows the rate of ADP
397 release, eliminates the ADP-release-associated tilting of the lever, and increases the rate of ATP
398 binding to rigor actomyo1c (16). To investigate the structural origins of this behavior, we solved
399 the cryo-EM structure of rigor (AM), actin-bound myo1c$^{\Delta N}$ (16) at a resolution of ~2.7 Å
400 (hereafter, referred to as 'myo1c$^{\Delta N}$ rigor'). This structure reveals that in the absence of an intact
401 NTE, the lever moves toward the motor domain, intruding into the space that in the wild-type

402 AM structure is occupied by the docked NTE. Loss of M1 results in disorder of part of loop-5
403 (72-75). Our structure model also indicates that E76 reorients to occupy the space vacated by
404 M1 (Fig. 4E; Fig. S10), although the E76 side chain itself is not directly visualized presumably
405 due to its net negative charge. Moving closer to the motor domain leads the myo1c$^{\Delta N}$ lever to
406 make a new putative interaction with loop-5 (E76-R639) in addition to the E76-R631 interaction
407 observed in the wild-type AM.

408 Notably, these changes in lever and loop-5 conformations in the myo1c$^{\Delta N}$ rigor structure
409 compared with wild-type rigor (AM), correlate with changes at the nucleotide pocket that
410 appear to regulate nucleotide affinity. The A-loop, which connects to the C-terminus of loop-5,
411 moves with the N-terminal subdomain domain (~1°) back toward the P-loop to allow formation
412 of the H-bond between N53 and the P-loop H-bond, thus restoring the H-bond interaction belt
413 that connects the switch-1, P-loop, A-loop. If this belt facilitates tight nucleotide binding to the
414 P-loop, loss of coupling to the lever/loop-5 in the myo1c$^{\Delta N}$ mutant may explain the enhanced
415 rate of ATP binding to myo1c$^{\Delta N}$ (see below).

416

417 **Modeling the power stroke of full length Myo1c**

418 We built a full length myo1c (FL-myo1c; Fig. 5) molecule allowing us to model the
419 trajectory of the power stroke using the previously determined crystal structure of the myo1c
420 tail domain that includes the lever arm helix and three bound calmodulins (PDB: 4R8G; (37)).
421 The region from the end of the tail to the motor domain does not contain hinges or regions of
422 substantial flexibility, suggesting that the myosin can be considered rigid between the actin-
423 and membrane-binding sites (Fig. 5).

424 Using the crystal structure of myo1c in the presence of Mg^{2+}·ADP·VO_4 (PDB: 4BYF; (28))
425 to represent the M.ADP.P_i state, we docked FL-myo1c on actin using the lower 50-kDa, that
426 includes loops-2 and -3, and monitored the lever position of the M.ADP.Pi, AM.ADP^A, AM.ADP^B,
427 to AM states (Fig. 5). In the pre-power-stroke state, the lever is nearly parallel to the long axis
428 of the actin helix. As the motor progresses from AM.ADP.Pi to AM.ADP^A the lever tilts ~50
429 degrees in the plane of the actin and then a further ~20° to the AM state, resulting in a lever
430 position that is nearly perpendicular to the actin filament (Fig. 5). This lever arm angle is very
431 different from other characterized myosins, and it may result in differences in how the motor
432 domain responds to forces aligned with the long axis of the actin filament. Additionally, it has
433 implications for motility relative to the cell membrane (see below).
434
435
436 **DISCUSSION**
437 In summary, we discovered that myo1c binds to actin in a unique orientation that
438 produces a 'skewed' power stroke, and that this skewing is further amplified by unique
439 structural features of the myo1c NTE. Together, these features may explain the motor's ability
440 to turn actin filaments in gliding assays (12, 13). We also found that the conformational
441 changes that myo1c undergoes to release ADP are substantially different from myo1b, and the
442 NTE has a unique structure. These differences may explain differences in force sensitivity.
443 Finally, our new structures allow us to model the working stroke of the full length myo1c
444 molecule, providing insights into function of the native molecule.
445

446 **Lever tilting and Force Dependence of ADP Release**

447 To initiate the myo1c lever swing from AM.ADP^{A} to AM.ADP^{B}, the L5–lever bridge that
448 connects loop-5 to the lever must break via isomerization of the F74 - Y75 side chain pair. The
449 disruption of this mechanical linkage, which does not happen in myo1b, evidently uncouples
450 the lever position from the nucleotide pocket conformation (Fig. 6; Movies S3-S4). Importantly,
451 we propose that breakage of the L5–lever bridge is rate limiting for the biochemically measured
452 ADP release step. Breakage of the L5–lever bridge would not be force sensitive as little lever
453 movement is required (Fig. 6A). Subsequent rotation of the N-terminal subdomain to a position
454 that allows nucleotide exchange occurs after the lever rapidly tilts and is stabilized by NTE
455 docking and formation of the arginine lock. This aspect of the mechanism is supported by our
456 myo1c$^{\Delta N}$ rigor structure, whose nucleotide pocket appears suited for stronger nucleotide
457 binding (i.e., formation of the H-bond interaction belt; Fig. 3G) despite a lever swing that is
458 largely complete. Moreover, biochemical studies of the myo1c$^{\Delta N}$ mutant revealed that in the
459 ADP state, most of the motor population released nucleotide much more slowly than wild-type,
460 indicating that ADP release was compromised.

461 In contrast to myo1c, myo1b maintains its L5–lever bridge throughout the transition
462 from the AM.ADP^{A} to AM states (Fig. 4F–G), which may result in continuous coupling between
463 the N-terminal subdomain and the position of the lever and converter (Fig. 6B; Movie S4).
464 Thus, we propose that the disruption of key bonds that hold ADP in the nucleotide pocket (due
465 to rotation of the N-terminal subdomain) is rate limiting and occurs when the lever has tilted to
466 the AM.ADP^{B} state. Thus, during the AM.ADP^{A} to AM.ADP^{B} lever swing the position of the
467 transition state would be near the AM.ADP^{B} state, resulting in a larger distance parameter and

468 increased force sensitivity of ATP-dependent actin detachment, as measured in the optical trap
469 (10, 11, 38). The transition between AM.ADP^{B} to AM corresponds to an oblique lever
470 movement (14) (Fig. 2F) that is likely to be rapid, and docking of the hydrophobic myo1b NTE is
471 initialized by docking of L10 and L11 in the AM.ADP^{A} state at the beginning of the lever swing.
472

473 **Novel compliant element in lever arm linkage**

474 We discovered a compliance in both myo1b and myo1c structures where the SH2 helix
475 connects to the converter. The short linking loop (Myo1c, F627-A628; Myo1b, A632-Y633)
476 found at this junction forms a key mechanical connection between the motor domain and the
477 lever. In other myosin structures (e.g., Myo5 and MYH7) this loop remains mostly rigid during
478 ADP release (Fig. S11), contributing to tight coupling between the nucleotide pocket and the
479 lever swing (39). However, in myo1c, sequence divergence resulting in an alanine (A628) in
480 place of a proline that is highly conserved in non-myosin-I families allows pronounced bending
481 of the SH2-converter linker during the ADP swing (Fig. S11). Nearly identical behavior is
482 observed in myo1b, although this was not previously reported (14). 'Unhinging' of this linker in
483 myo1b and myo1c likely facilitates the unique lever positions and tilting angles of myosin-I
484 paralogs.
485

486 **Effect of the NTE on ATP binding**

487 Although the transition of myo1c from the AM.ADP^{B} state to AM is accompanied by only
488 a minor (1°) rotation of the N-terminal subdomain, it is accompanied by a slight expansion (or
489 breathing) of the N-terminal subdomain that disrupts the H-bond interaction belt, resulting in a

490 conformation that likely does not tightly bind nucleotide. This finding may explain an
491 interesting effect on ATP-binding kinetics observed for myo1c. Stopped-flow experiments
492 reveal that rigor myosin exists in two states that are in equilibrium; one that binds ATP and
493 another that does not bind ATP, with the non-binding state predominating by more than 3-fold
494 (8, 9). An isomerization in actomyo1c must therefore occur for the ATP to bind; our inability to
495 obtain distinct structures of these two populations from our rigor samples by cryo-EM
496 classification indicates that the structure differences between them must be relatively subtle.
497 Given its kinetic predominance, our wild-type myo1c cryo-EM AM structure likely
498 represents the conformation that does not bind readily ATP, consistent with our finding of a
499 more open active site. Strikingly, removal of the myo1c NTE results in a biochemical
500 equilibrium of actin-bound myo1c$^{\Delta N}$ that favors the state that can bind ATP (16). Indeed, our
501 cryo-EM structure of myo1c$^{\Delta N}$ shows a reorientation of the N-terminal subdomain that restores
502 the H-bond interaction belt and re-closes the nucleotide pocket, which is a state that we predict
503 will bind nucleotide tightly. By this interpretation, loosening of the active site by the NTE would
504 tend to accelerate ADP release while simultaneously discouraging ATP binding, consistent with
505 biochemical observations.

506 **Origins of force sensitivity in the ATP binding step**

507 ATP binding by myosin-I's is divided into two steps: an initial isomerization in the AM
508 state that permits formation of a weak-ATP binding complex, and a second isomerization to a
509 strong ATP-binding state. As already discussed, the first of these isomerizations likely involves a
510 minor 'breathing' movement of the nucleotide active site that enables ATP to interact with the
511 P-loop (Fig. 3F), minimal lever movement (Fig. 1B-C), and is not associated with force sensitivity.

512 The second isomerization, which is linked to force sensitivity by optical trapping and
513 biochemical data (8), has not been characterized structurally but likely involves a 'post-rigor'
514 conformation captured in X-ray studies of several other myosins (31, 40, 41). In the post-rigor
515 conformation, the nucleotide pocket closes to interact tightly with ATP, accompanied by
516 movement of the upper-50 kDa domain that weakens the actin interface in preparation for
517 ATP-induced detachment.

518 To investigate how force sensitivity may be linked with the second ATP-isomerization,
519 we compared our AM myo1c cryo-EM structures with an AlphaFold-generated model of post-
520 rigor ATP-bound myo1c (Uniprot Q5ZLA6x) (42). The AlphaFold model exhibits an
521 approximately rigor-like lever position with a docked NTE (Movie S3). However, unlike AM
522 myo1c or myo1b structures, the AlphaFold post-rigor model does not show 'unhinging' of the
523 SH2-converter linking loop (Fig. S11); thus, the coupling pathway from the lever to the
524 nucleotide pocket partially reverts back to the AM.ADP^{A} arrangement in the Alphafold model.
525 Moreover, the Alphafold model shows little lever angle change compared with AM. This
526 contradicts optical trapping force sensitivity measurements, which seem to require that an
527 additional lever movement accompanies the weak-to-strong ATP isomerization (15, 16).

528 It therefore seems likely that the AlphaFold post-rigor myo1c model does not fully
529 capture the weak to strong ATP-binding isomerization. We speculate that myo1c nucleotide
530 pocket closure may be accompanied by lever rotation somewhat beyond the rigor-like position
531 observed in the AlphaFold model, dislodging (or otherwise introducing strain in) the docked N-
532 terminal extension. A resisting load that drives the lever from this 'strong-ATP' position back
533 towards AM would thus favor NTE docking and disfavor strong ATP binding, explaining why this

534 step is force-sensitive. The same mechanism would also explain the observation that deleting
535 the myo1c NTE greatly accelerates the weak-to-strong ATP binding transition (16), since this
536 deletion would allow the motor to more freely fluctuate to the strong ATP-binding
537 conformation.
538
539 **The power stroke of full length myo1c**
540 The ability to model the overall power stroke of full length myo1c is an exciting and
541 revealing outcome of this work (Fig. 5). Like most myosins, the lever tilts toward the barbed
542 end of the actin filament (27); however, myo1c starts in the AM.ADP.Pi state in an orientation
543 nearly parallel to the actin filament and progresses to a point that is just past perpendicular.
544 This tilting trajectory is very different from other myosins, where the lever ends in an
545 orientation tilted more towards the barbed end, which leads to the question of why myosin-I
546 evolved this structural adaptation.
547 A pleckstrin homology (PH) domain in the myo1c tail domain binds directly to
548 phosphoinositides in the lipid membranes (43, 44), so it is relevant to consider the working
549 stroke in relation to the plane of the membrane (Fig. 5). If myosin binds to actin filaments that
550 are fixed in an orientation parallel to the plane of the membrane, the power stroke results in a
551 10 nm displacement perpendicular to the actin and membrane, resulting in separation of the
552 actin and membrane (Fig. 5B). Alternatively, if the motor is more rigidly fixed to the
553 membrane, the motor could bring the barbed end of the actin filament closer to the membrane
554 (Fig. 5C). This geometry may effectively position the barbed-end of actin to allow

555 polymerization forces to push the membrane. Indeed, *in vitro* experiments show that myosin-I
556 can synergize with Arp2/3 complex to enhance the pushing forces of myosin-I (45).
557 Finally, the striking finding that myo1c perches on actin at a different angle from other
558 myosins suggests a mechanism for the asymmetric gliding of actin filaments observed in
559 motility assay (12, 13). Experiments in *Drosophila* suggest a role for the myosin-I motor domain
560 in establishing cell and organ chirality during development (13); however, it remains to be
561 determined if the modulation of chiral activity is due to this torque or to modulation of motor
562 kinetics (46). Interestingly, a low resolution structure of actin-bound *Acanthamoeba* myosin-IB
563 also reveals an altered actin perch (25). Thus, this feature has been conserved, so future cell
564 biological experiments will be required to determine the mechanistic role for this structure.
565
566

Acknowledgements

We thank Dr. Daniel Safer and Rick Wike for assistance with protein expression and purification. We would like to acknowledge Dr. Shenping Wu and the Yale Cryo-EM Resource, as well as the Yale Center for Research Computing facility for expert support and maintenance of these facilities. Data collection at Penn was performed at the Electron Microscopy Resource Lab and The Beckman Center for Cryo-Electron Microscopy, University of Pennsylvania (Research Resource Identifier SCR_022375). This work was supported by NIH Grants R01 GM110530 to CVS and R37 GM057247 to EMO, and the National Science Foundation CMMI Grant 15-48571 to EMO. Finally, we would like to thank the reviewers for insightful and helpful comments, which led to new insights and significantly improved the manuscript.

Data availability

Atomic coordinates and corresponding cryo-EM density maps, including the half maps, masks and FSC curves used to estimate spatial resolution have been deposited in the Protein Data Bank (PDB) and Electron Microscopy Data Resource (EMD) under the accession codes 9CFU/EMD-45563 (myo1c AM.ADP^{A} actin complex), 9CFW/EMD-45565 (myo1c AM.ADP^{B} actin complex), 9CFX/EMD-45566 (wild-type myo1c rigor actin complex, or AM), and 9CFV/EMD-45564 (myo1c$^{\Delta N}$ rigor actin complex).

Code availability

587 A python script was written for UCSF ChimeraX to perform lever swing analyses and

588 visualizations in Fig. 2, Supplementary Fig. 7, Supplementary Tables S5 and S6. The script is

589 publicly available on gitlab (https://gitlab.com/cvsindelar/lever-swing).

590 **METHODS**

591 **Protein Preparation**

592 The short, mouse, splice isoform of Myo1C containing the amino-terminus ([1]MESALT…)
593 through all three IQ domains (residues 1-767) immediately followed by the sequence
594 GGLNDIFEAQKIEWHEAADYKDDDDK that includes a BirA biotinylation site (AviTag;
595 GLNDIFEAQKIEWHE) and a FLAG epitope tag (DYKDDDDK) for purification, was expressed using
596 the Sf9-baculovirus system (43). The myo1c$^{\Delta N}$ expression construct was identical to myo1c,
597 except for the removal of the NTE (E2-V10) as described (16). Myosin was purified by FLAG-
598 affinity and ion exchange as previously described(8, 16, 47). Rabbit skeletal muscle actin was
599 purified as previously described (48). Actin polymerization was induced by adding 0.1 volume of
600 10x KMEI buffer (500 mM KCl, 20 mM $MgCl_2$, 10 mM EGTA, 100 mM imidazole, 20 mM ATP, 2
601 mM DTT) to ~5 µM of G-actin at room temperature for 1 hour. Actin filaments were stabilized
602 using phalloidin at 4 C overnight. Actin filaments were collected by ultracentrifugation
603 (Beckmann Rotors, TLA 120.1, 70000 x g, 30 minutes at 4 C) and the pellet was resuspended in
604 F-actin buffer (10 mM HEPES pH 7.5, 100 mM KCl, 2 mM $MgCl_2$, 1 mM DTT). Then, F-actin was
605 incubated with excess myo1c for 1 hour on ice. Actomyosin filaments were collected as a pellet
606 by ultracentrifugation (Beckmann Rotors, TLA 120.1, 70000 x g, 1 hour at 4 C). The pellet was
607 resuspended in F-actin buffer (10 mM HEPES pH 7.5, 100 mM KCl, 2 mM $MgCl_2$, 1 mM DTT) at a
608 concentration of 2-5 mg/mL before grid preparation. The myo1c-ADP samples were prepared
609 by dissolving the pellets in F-actin buffer containing 1 mM K_2ADP.

610

611 **Sample freezing and data collection**

612 Samples were frozen on Quantifoil 1.2/1.3 300-mesh (Holey carbon) copper grids; to
613 enhance filament decoration, grids were not glow-discharged but were blotted specially to
614 improve ice quality (49). A sample of 3.0 µL was applied onto the carbon side of the grid using
615 FEI Vitrobot™ Mark IV at 4°C and 100% humidity. The samples were incubated on the grid for
616 50 s and the extra solution was blotted using two Vitrobot filter papers (Ø.55/20 mm, Grade
617 595, Ted Pella) for 4 s at 0 blot force. The grids were plunged into liquid ethane at ~180 °C with
618 a wait time of 0.5 s. The vitrified grids were screened for sample homogeneity and ice thickness
619 in a Glacios 200 kV transmission electron microscope equipped with Gatan K2 summit camera.
620 Electron micrographs for image reconstructions were collected using a Titan Krios at 300 kV,
621 with a Gatan image filter with slit width of 20 eV in nanoprobe mode. The ADP data set was
622 collected using the Krios in the Yale cryo-EM facility, while the two other data sets (wild-type
623 and myo1c$^{\Delta N}$ rigor) were collected with at the UPenn Singh center Krios; both microscopes
624 were equipped with a cold-field emission gun. A K3 Gatan summit camera in super-resolution
625 mode was used to collect 1 movie per hole (using serialEM data collection software and EPU
626 software at the Yale and Penn facilities, respectively). The target defocus range was between -
627 2.5 µm and -1.2 µm.
628 The ADP data set was collected at a nominal magnification of 64K (Yale Krios, GIF plus
629 K3), and cryo-EM structure refinement was carried out using a nominal pixel size of 1.386 Å.
630 The wild-type rigor data set (AM) was collected at a nominal magnification of 64K (UPenn Krios,
631 GIF plus K3) and cryo-EM structure refinement was carried out using a nominal pixel size of 1.36
632 Å. The myo1c$^{\Delta N}$ rigor data set was collected at a nominal magnification of 81K (UPenn Krios, GIF
633 plus K3) and cryo-EM structure refinement was carried out using a nominal pixel size of 1.08 Å.

634 All images were recorded in super-resolution mode. Exposure information for the three
635 datasets is as follows. ADP movies: 40 frames, total dose of 52 counts/Å^2, total of 3800
636 exposures; WT rigor movies: 45 frames, total dose 50 counts/ Å^2, total of 3673 exposures;
637 myo1c$^{\Delta N}$ rigor movies: 40 frames, total dose of 50 counts/ Å^2, total of 3704 exposures. Frame
638 exposure duration for the three data sets was 0.065 - 0.13 sec/frame.

639 All datasets were processed entirely using CryoSPARC v3 (50). Micrographs were
640 subjected to motion correction (Patch Motion Correction) and CTF estimation before particle
641 picking. Filaments were selected using the cryosparc 'Filament Tracer' function. After
642 extraction, particle stacks were subjected to 2-D classification to remove non-filamentous
643 particles. The resulting particles (3088218, 2667431, and 2548251 total particles for ADP, WT
644 rigor, and myo1c$^{\Delta N}$ rigor datasets, respectively) were then subjected to helical refinement,
645 followed by optical parameter refinement including defocus and magnification anisotropy.
646 Next, single-particle refinement was performed with a particle-subtracted image stack using a
647 focusing mask comprising the central ~5 actomyosin subunits. Finally, local refinement was
648 performed using a focusing mask comprising the central myosin subunit plus its neighboring
649 actin trimer. Global resolution estimates for the resulting homogeneous reconstructions (actin
650 plus myosin) were ~2.7 - 2.8 Å for each of the three data sets.

651 Multiple attempts were made to identify conformational sub-populations. Focused
652 classification with particle subtraction using various target regions, including the lever and N-
653 terminal extension, failed to identify discrete conformational classes. Variability analysis, also
654 using a variety of different focusing masks, was tried on all three data sets but discrete classes
655 were only identified in the ADP data set. The target region for this latter case was a low-

656 resolution mask encompassing the lever arm. Two sequential variability analysis steps were
657 required to obtain well-defined maps for ADP A and ADP B structures (Fig. S4). In the first step,
658 non-occupied myosin sites were sorted out and a relatively pure population (cluster) of 671620
659 ADP A particles was identified (Fig. S4A - C). Lever density in one of the other identified sub-
660 populations from this first step appeared to reflect a mixture of lever conformations, and was
661 subjected to a second round of variability analysis. This second step yielded a sub-population of
662 126845 particles with relatively well-defined lever density corresponding to the ADP B structure
663 (Fig. S4D–E). To reduce potential bias due to masking and other artifacts, variability analysis was
664 performed using alignments obtained prior to the final local refinement step (one myosin plus
665 actin-trimer mask), while final 3D reconstructions for ADP structural states were obtained from
666 particle alignments obtained from the final local refinement step (note that this was a global
667 alignment with all 3088218 particles from the ADP dataset).
668 Following refinement, the resulting volume pixel sizes were adjusted to the most
669 accurate available values. For the ADP data set, a calibrated pixel size of 1.346 Å was used (37),
670 giving an actin repeat spacing of 27.47 Å (ADP A) and 27.37 Å (ADP B). Actin repeat distances
671 were estimated using the 'measure rotation' command of UCSF ChimeraX, applied to an
672 identical actin subunit PDB model fit into two different subunit sites in the density maps (51).
673 For the myo1c$^{\Delta N}$ rigor structure, final 3D reconstructions were adjusted to a calibrated pixel size
674 of 1.068 Å (38), giving an actin repeat distance of 27.41 Å. For the WT rigor data set, the pixel
675 size was adjusted so that the resulting actin repeat spacing matched that in the ADP
676 reconstruction: a value of 1.332 Å was selected, giving an actin repeat distance of 27.44 Å. Note
677 that this pixel size is significantly smaller than the calibrated size we used for the ADP data set,

678 which was collected with similar instrument settings but a different microscope (Yale vs. UPenn
679 Krios). This discrepancy may therefore be due to differing instrument calibrations for the two
680 microscopes. Alternatively, it is possible for example that the calibrated pixel size (1.346 Å) is
681 accurate for both microscopes, which would mean that that myo1c ADP release triggers a 1%
682 increase in actin spacing. Conclusions of the current work are not affected by this choice of
683 pixel size.

684 Initial structure models were built using the model-angelo automated tool (52), and
685 further building and refinement was done manually using Isolde (53), COOT (54) and Phenix
686 (55); Isolde was used for the final refinement cycles. Figures were generated using ChimeraX
687 (56).

688

689 **Figure legends**

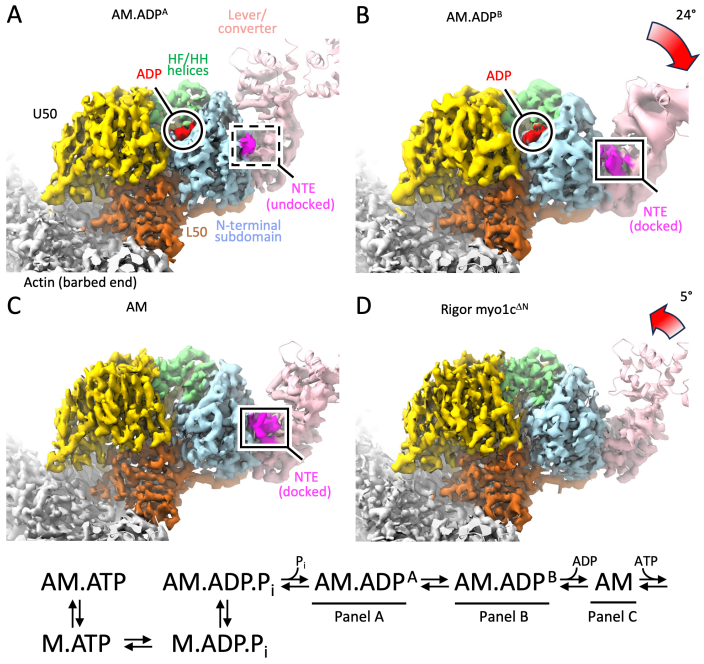

690

691 Fig. 1. ADP-dependent lever swing of myo1c revealed by near-atomic cryo-EM structures. (*A*)
692 View of the 2.8 Å resolution structure of actin-bound ADP myo1c, in the AM.ADP^{A} state. The
693 actin barbed-end points out of the page, slightly obliquely, toward the reader. Myosin
694 subdomains are color coded as: (yellow) upper-50 kDa domain; (caramel) lower 50-kDa domain;
695 (light blue) N-terminal subdomain; (light green) HF and HH helices; (light pink) lever arm plus
696 converter; (red) ADP; (magenta) N-terminal extension. Only a few C-terminal residues of the
697 NTE are ordered (dashed box). (*B*) Cryo-EM structure of the myo1c AM.ADP^{B} state with
698 identical coloring and view as AM.ADP^{A}. The lever arm swings 24° relative to AM.ADP^{A}, and
699 density for docked NTE bridges between the lever and the N-terminal subdomain. (*C*) AM state
700 of myo1c cryo-EM structure, showing a lever position very similar to AM.ADP^{B}. (*D*) AM myo1c$^{\Delta N}$
701 cryo-EM structure, showing a lever that reorients ~7° back towards the AM.ADP^{A} position
702 compared with wild-type. Density maps are shown as colored isosurfaces superposed on the

703 molecular models, which are rendered with ribbon cartoons. To improve visibility of lever

704 features, the isosurface contour threshold level is locally decreased in all four panels (see Fig.

705 S1). The actomyosin ATPase scheme is shown with correlated structural states identified by

706 figure panel.

707

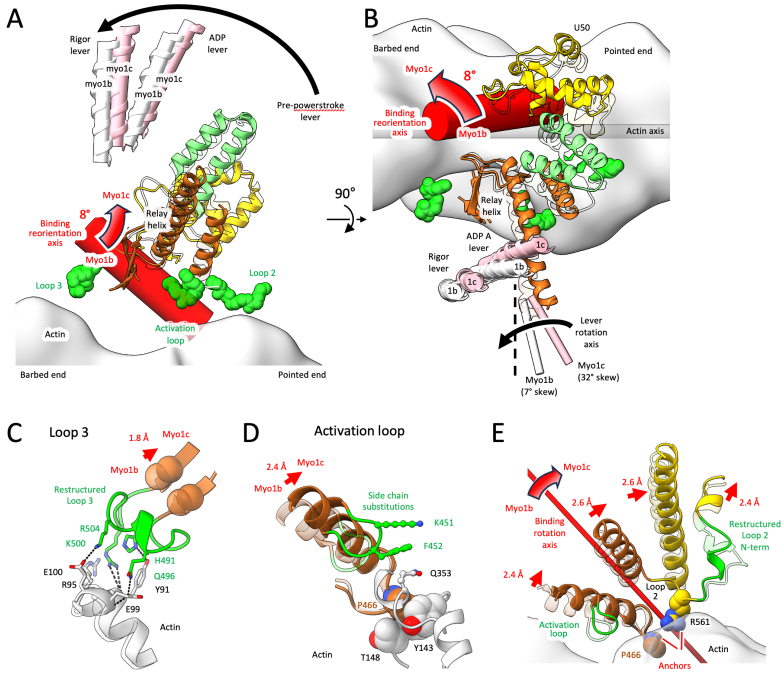

Fig. 2. Structural origin of a skewed lever swing in myo1c. See also Figs S6 and S7 and movies S0 and S1. (*A*) Side view of acto-myo1c (actin axis is horizontal) showing eight-degree rotation of the myo1c motor domain on actin compared with myo1b. Myo1b (14) (transparent ribbons) and myo1c cryo-EM structures (colored ribbons) are aligned by their central three actin subunits. Starting from this alignment, a thick red cylinder depicts the binding reorientation axis required for least-squares superposition of rigor myo1b upper and lower 50-kDa domains onto myo1c; the axes for ADP-state superpositions are similar (not shown). The reorientation tilts the lever arm helix (pink ribbons with cylinders running through them, and white ribbons and cylinders for myo1c and myo1b, respectively) towards the actin pointed-end. Three myosin loops whose actin contacts are linked to the binding orientation change are depicted as green van der Waals spheres. Full details of the binding reorientation axis calculation are given in the Movie S1 caption. (B), Orthogonal view of (A) revealing that the ADP lever arm swing of myo1c is more skewed (larger off-axis component) than myo1b. Lever rotation axes defining the hinge

722 points of the myo1b and myo1c ADP lever swings are depicted as thin cylinders, colored white
723 and pink, respectively. Full details of lever arm rotation axis estimation are given in Fig. S7. For
724 reference, the black vertical dashed line denotes a lever rotation axis with no off-axis
725 component (*C*) Restructuring of myo1c loop-3 that accommodate its repositioning on the actin
726 surface compared with myo1b (see Fig. S6A). In this and the following panels, structure
727 alignments are the same as (*A*)–(*B*) and the viewing angles are close to *(A*), but individually
728 adjusted for best viewing of selected elements*.* (*D*) Side chain substitutions in the myo1c
729 activation loop that accommodate its repositioning on the actin surface compared with myo1b
730 (see Fig. S6B). (E) Restructuring of myo1c loop-2 accommodates the orientation change (see
731 Fig. S6C–D and Movie S2). Conserved side chains that serve as anchor pivots for the myo1b to
732 myo1c re-orientation are represented using van der Waals spheres. Note that, different to the
733 Fig. 2A-B, the binding reorientation axis is rendered in this panel as a thin rather than thick
734 cylinder
735

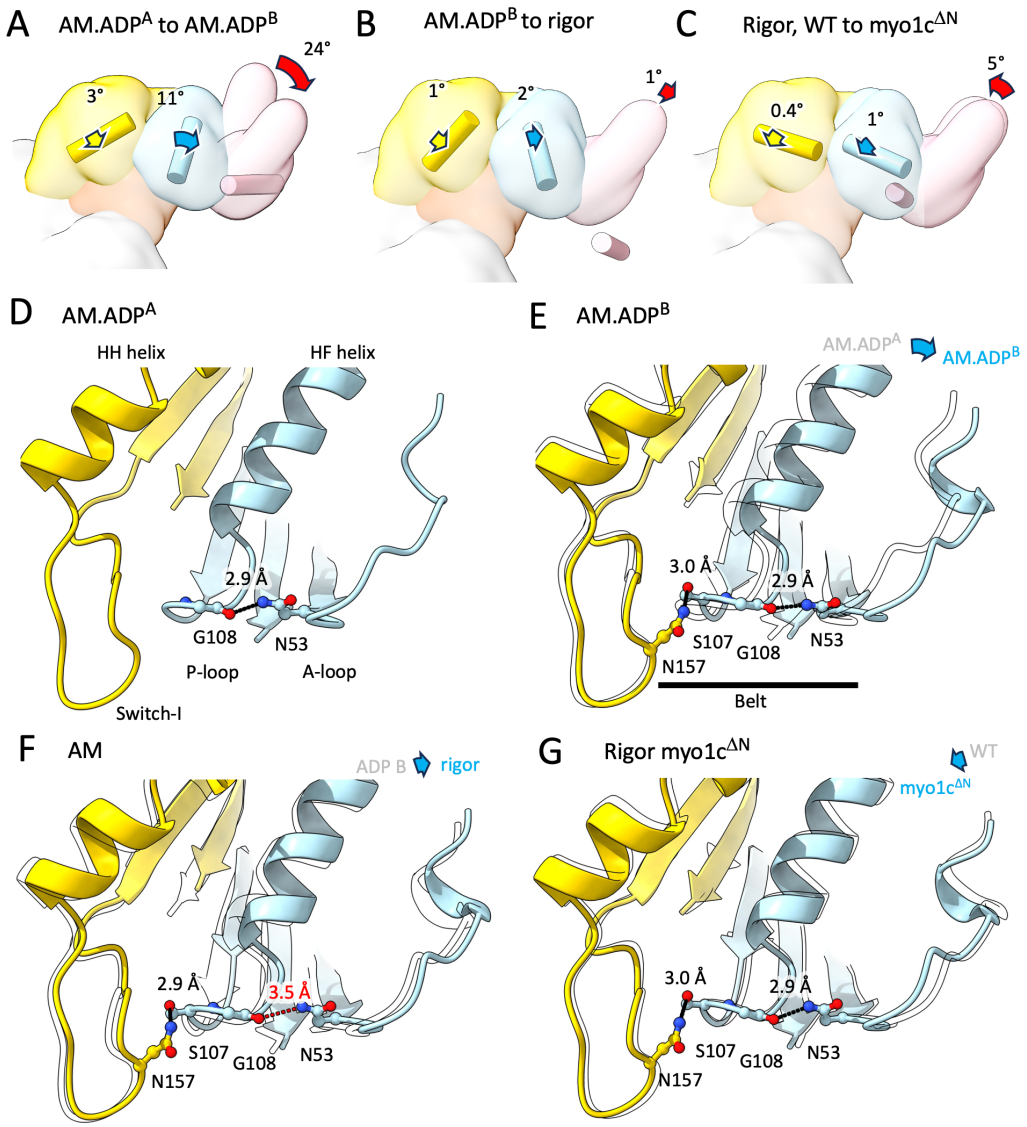

Fig. 3. Nucleotide-dependent domain movements related to ADP release from actin-bound myo1c. (*A*) Subdomain rotations comparing our AM.ADP^{A} and AM.ADP^{B} structures, from a reference alignment where lower 50 kDa subdomains are superimposed. The myo1c lever/converter and other domains are represented as isosurfaces of 16 Å resolution synthetic density maps generated from our atomic models of AM.ADP^{A} and AM myo1c; domains are colored as in Fig. 1. Colored cylinders depict the rotation axis required to superimpose respective myo1b and myo1c subdomains with respect to the reference alignment. Colored

744 arrows denote the rotation direction. Subdomains rotate very little except for the (pink)
745 lever/converter where a significant lever swing is evident. The lever rotation axis (pink colored
746 cylinder) is positioned at the structural hinge location as in Fig. 2A-B. The remaining rotation
747 axes are positioned at the respective subunit centers of mass. (*B*-*C*) Analysis as in (*A*) showing
748 that nucleotide-binding subdomain rotations going from AM.ADP^{B} to AM are subtle and are
749 partially reversed in the AM myo1c$^{\Delta N}$ structure. (*D*-*G*) Details of the nucleotide pocket for the
750 four myo1c structures. Atomic models are rendered as ribbon cartoons with stick models for
751 selected residues; reference ribbon structures corresponding the comparisons in (*A*-*C*) are
752 overlayed as transparent silhouettes. Strained H-bond between the P-loop and A-loop is
753 colored red in (*F*). Subdomain rotations and shifts were estimated using published python
754 scripts (51) within UCSF ChimeraX (57).

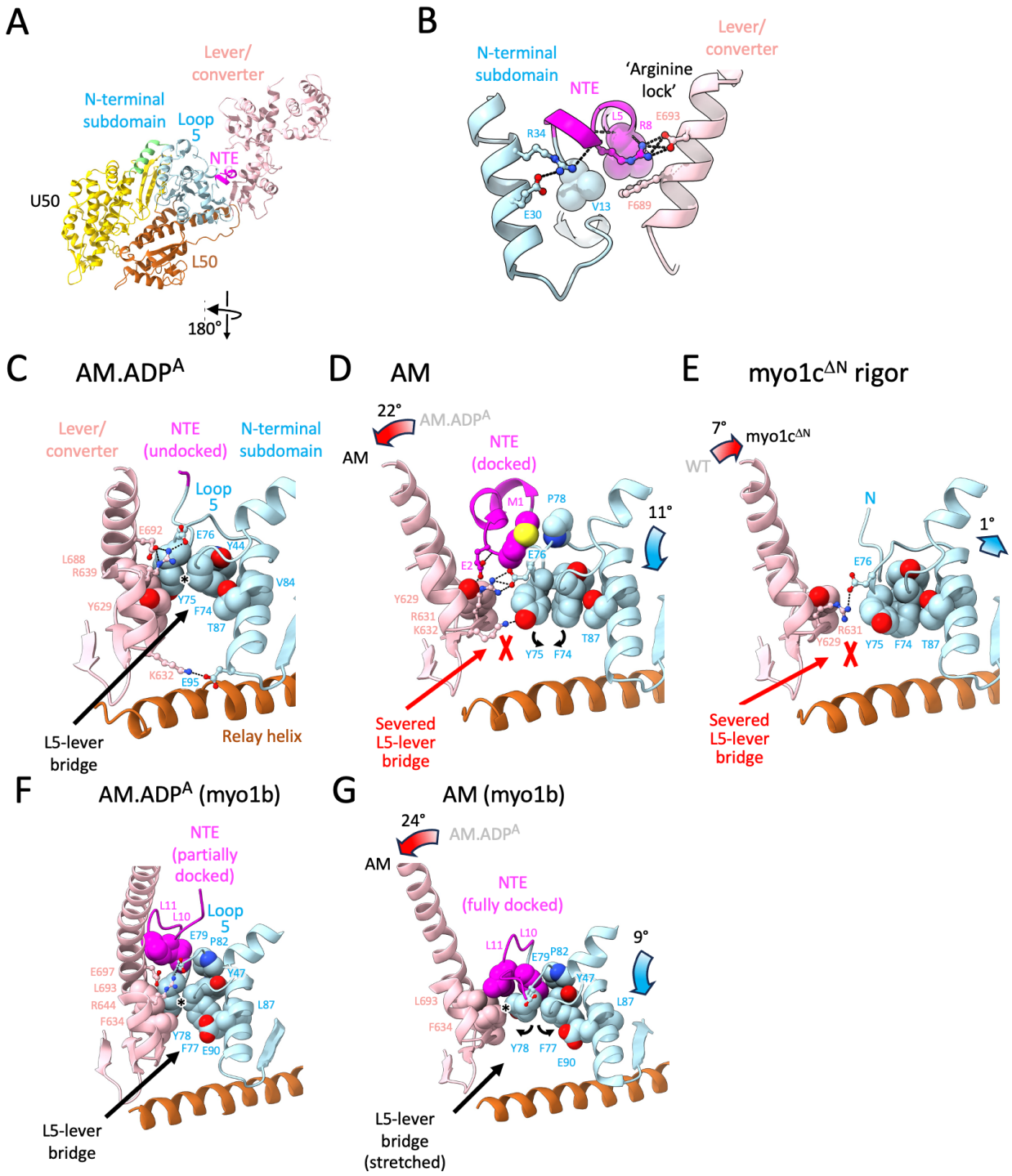

755

756 Fig. 4. Conformational changes in the myo1c and myo1b lever arm and N-terminal extension

757 associated with ADP release and force-sensitivity. (*A*) Overview of the myo1c structure, shown

758 in the AM state with a docked N -terminal extension; viewing angle and coloring are the same

759 as in Figs. 1 and 3. (*B*) Close-up of the docked N-terminal extension in (*A*), highlighting
760 electrostatic interactions (ball-and-stick-rendered side chains) unique to myo1c that lock the
761 lever orientation with respect to the N-terminal subdomain, including a cation-pi stacking
762 interaction between R8 in the NTE and F689 in the lever. A hydrophobically interacting side
763 chain pair is depicted using VDW spheres. (*C* - *E*) Angle-dependent changes in lever-motor
764 domain interactions for different myo1c conformational substates. View is of the same region
765 as in (*B*), but from the opposite side (180° rotation around y). Residues depicted as VDW
766 spheres are involved in a hydrophobic contact bridge ('L5–lever bridge') between the lever and
767 loop-5, which severs upon lever rotation from the (*C*) AM.ADP^{A} to (*D*) AM states. Curved arrows
768 indicate interaction changes of residue pair F74-Y75 in loop-5. Cryo-EM density in this region of
769 the AM structure is essentially indistinguishable from the AM.ADP^{B} structure (Fig. S10). (*E*)
770 Myo1c$^{\Delta N}$ AM state. (*F* - *G*), Corresponding region in myo1b AM.ADP^{A} and AM structures (14),
771 showing that the L5–lever bridge distorts but does not break during ADP release.
772

773

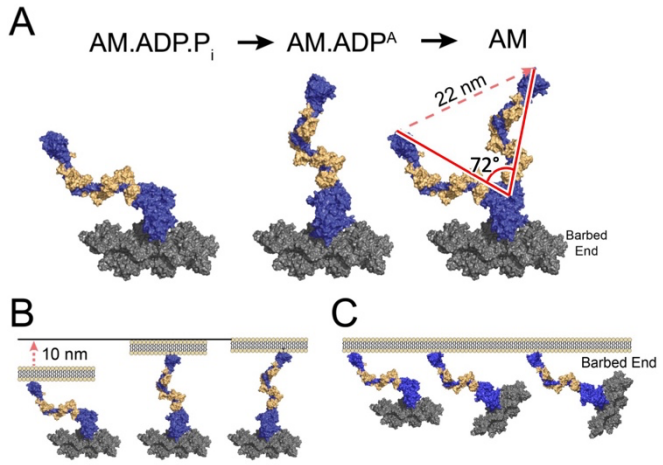

774 Fig. 5. Full-length myo1c model complexed with actin suggests roles in membrane remodeling.

775 (*A*) VDW sphere representation depicting the two-step lever swing associated with P_i release

776 and ADP release. The myo1c ADP•P_i state is represented by the crystal structure of a myo1c

777 vanadate co-complex (PDB: 4BYF; (28)); this structure is docked to actin by aligning the lower

778 50 kDa subdomain with our AM structure. (*B* – *C*) Putative motion of myo1c and actin during

779 the power stroke when the myo1c tail is anchored to a membrane, as inferred from the

780 structures in (*A*). (*B*) If the actin filament orientation is held fixed with respect to the

781 membrane, the power stroke translocates the actin filament parallel to the membrane. (*C*) If

782 the myo1c tail orientation is held fixed with respect to the membrane, the power stroke rotates

783 the filament, swiveling the barbed end towards the membrane.

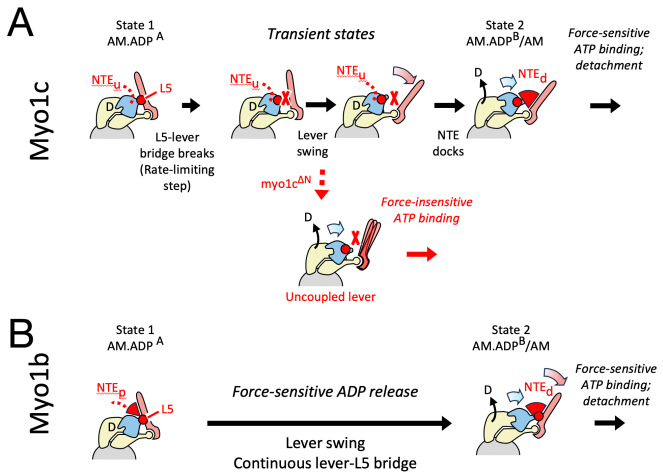

Fig. 6. Schematic model of force-mediated nucleotide exchange in actin-bound myo1c and myo1b. (*A*) Force-insensitive ADP release and force-sensitive ATP binding in myo1c. The ADP lever swing is proposed to consist of several force-insensitive substeps: (1) slow detachment of the lever from loop-5 with little lever movement, possibly initiated by isomerization of F77-Y78 in loop-5 (Fig. 4); (2) ADP lever swing, uncoupled from the nucleotide pocket conformation due to plasticity in the loop that connects the converter to SH2 in the motor domain (see Fig. S11); (3) docking of the N-terminal extension, which bridges between the lever and the motor domain and opens the nucleotide pocket slightly to accelerate ADP release (Fig. 3). The undocked or docked NTE is depicted as a dashed red line (labeled 'N_u') or red-colored wedge ('N_d'), respectively. In the absence of the N-terminal extension (Myo1c$^{\Delta N}$; bottom cartoon in panel A), opening of the nucleotide pocket is destabilized, introducing a sub-population that releases ADP slowly. Following ADP release, the docked N-terminal extension tightly couples lever position to nucleotide pocket conformation in the wild-type motor. This confers force-sensitivity to subsequent motor isomerizations that accompany ATP binding, likely involving

800 further movement of the lever that has not been visualized (15). Lacking a docked NTE, ATP
801 binding is uncoupled from lever movement in Myo1c$^{\Delta N}$, eliminating force sensitivity. (*B*) Model
802 for force-sensitive ADP release and ATP binding in myo1b. Unlike myo1c, the lever maintains
803 continuous contact with loop-5 in the motor domain during the ADP lever swing, which is
804 proposed to impart force-sensitivity to this step. The myo1b N-terminal extension also has a
805 different role than in myo1c, maintaining interactions with the hydrophobic bridge throughout
806 ADP release and 'catalyzing' this step by preferentially stabilizing the transition state (presumed
807 similar to AM.ADP^{B}) and final state (AM) over the AM.ADP^{A} state. The red X's between motor
808 domain and lever (panel A, top row, middle two states) denote severing of the ϕ-bridge. The
809 partially docked myo1b NTE in the ADP^{A} state is depicted as a small red-colored wedge and a
810 dashed red line (labeled 'N_p'), while the fully docked myo1b NTE is depicted as a larger red-
811 colored wedge ('N_d'). Note that AM.ADP^{B} and AM structures are combined as a single depicted
812 image in (A) and (B); this transition is unlikely to contribute to force sensitivity due to minimal
813 motion of the lever in either myo1b or myo1c.
814

815 **References**

816 1. M. J. Greenberg, G. Arpag, E. Tuzel, E. M. Ostap, A Perspective on the Role of Myosins as
817 Mechanosensors. *Biophys J* **110**, 2568-2576 (2016).
818 2. S. M. Heissler, J. R. Sellers, Kinetic Adaptations of Myosins for Their Diverse Cellular
819 Functions. *Traffic* **17**, 839-859 (2016).
820 3. E. M. De La Cruz, E. M. Ostap, Relating biochemistry and function in the myosin
821 superfamily. *Curr Opin Cell Biol* **16**, 61-67 (2004).
822 4. B. B. McIntosh, E. M. Ostap, Myosin-I molecular motors at a glance. *J Cell Sci* **129**, 2689-
823 2695 (2016).
824 5. M. J. Greenberg, E. M. Ostap, Regulation and control of myosin-I by the motor and light
825 chain-binding domains. *Trends Cell Biol* **23**, 81-89 (2013).
826 6. J. H. Lewis, T. Lin, D. E. Hokanson, E. M. Ostap, Temperature dependence of nucleotide
827 association and kinetic characterization of myo1b. *Biochemistry* **45**, 11589-11597
828 (2006).
829 7. L. M. Coluccio, M. A. Geeves, Transient kinetic analysis of the 130-kDa myosin I (MYR-1
830 gene product) from rat liver. A myosin I designed for maintenance of tension? *J Biol*
831 *Chem* **274**, 21575-21580 (1999).
832 8. M. J. Greenberg, T. Lin, Y. E. Goldman, H. Shuman, E. M. Ostap, Myosin IC generates
833 power over a range of loads via a new tension-sensing mechanism. *Proc Natl Acad Sci U*
834 *S A* **109**, E2433-2440 (2012).
835 9. C. Batters *et al.*, Myo1c is designed for the adaptation response in the inner ear. *Embo J*
836 **23**, 1433-1440 (2004).
837 10. J. M. Laakso, J. H. Lewis, H. Shuman, E. M. Ostap, Myosin I can act as a molecular force
838 sensor. *Science* **321**, 133-136 (2008).
839 11. J. M. Laakso, J. H. Lewis, H. Shuman, E. M. Ostap, Control of myosin-I force sensing by
840 alternative splicing. *Proc Natl Acad Sci U S A* **107**, 698-702 (2010).
841 12. S. Pyrpassopoulos, E. A. Feeser, J. N. Mazerik, M. J. Tyska, E. M. Ostap, Membrane-
842 bound myo1c powers asymmetric motility of actin filaments. *Curr Biol* **22**, 1688-1692
843 (2012).
844 13. G. Lebreton *et al.*, Molecular to organismal chirality is induced by the conserved myosin
845 1D. *Science* **362**, 949-952 (2018).
846 14. A. Mentes *et al.*, High-resolution cryo-EM structures of actin-bound myosin states reveal
847 the mechanism of myosin force sensing. *Proc Natl Acad Sci U S A* **115**, 1292-1297 (2018).
848 15. H. Shuman *et al.*, A vertebrate myosin-I structure reveals unique insights into myosin
849 mechanochemical tuning. *Proc Natl Acad Sci U S A* **111**, 2116-2121 (2014).
850 16. M. J. Greenberg, T. Lin, H. Shuman, E. M. Ostap, Mechanochemical tuning of myosin-I by
851 the N-terminal region. *Proc Natl Acad Sci U S A* **112**, E3337-3344 (2015).
852 17. J. Robert-Paganin *et al.*, Plasmodium myosin A drives parasite invasion by an atypical
853 force generating mechanism. *Nature communications* **10**, 3286 (2019).
854 18. S. Fujita-Becker *et al.*, Functional characterization of the N-terminal region of myosin-2. *J*
855 *Biol Chem* **281**, 36102-36109 (2006).
856 19. P. D. Coureux *et al.*, A structural state of the myosin V motor without bound nucleotide.
857 *Nature* **425**, 419-423 (2003).

858 20. C. Veigel, J. E. Molloy, S. Schmitz, J. Kendrick-Jones, Load-dependent kinetics of force
859 production by smooth muscle myosin measured with optical tweezers. *Nat Cell Biol* **5**,
860 980-986 (2003).
861 21. M. J. Greenberg, H. Shuman, E. M. Ostap, Inherent force-dependent properties of beta-
862 cardiac myosin contribute to the force-velocity relationship of cardiac muscle. *Biophys J*
863 **107**, L41-44 (2014).
864 22. M. S. Woody, D. A. Winkelmann, M. Capitanio, E. M. Ostap, Y. E. Goldman, Single
865 molecule mechanics resolves the earliest events in force generation by cardiac myosin.
866 *eLife* **8** (2019).
867 23. M. Capitanio *et al.*, Ultrafast force-clamp spectroscopy of single molecules reveals load
868 dependence of myosin working stroke. *Nat Methods* **9**, 1013-1019 (2012).
869 24. C. Veigel, S. Schmitz, F. Wang, J. R. Sellers, Load-dependent kinetics of myosin-V can
870 explain its high processivity. *Nat Cell Biol* **7**, 861-869 (2005).
871 25. J. D. Jontes, E. M. Ostap, T. D. Pollard, R. A. Milligan, Three-dimensional structure of
872 Acanthamoeba castellanii myosin-IB (MIB) determined by cryoelectron microscopy of
873 decorated actin filaments. *J Cell Biol* **141**, 155-162 (1998).
874 26. J. Robert-Paganin *et al.*, The actomyosin interface contains an evolutionary conserved
875 core and an ancillary interface involved in specificity. *Nature communications* **12**, 1892
876 (2021).
877 27. J. Robert-Paganin, O. Pylypenko, C. Kikuti, H. L. Sweeney, A. Houdusse, Force Generation
878 by Myosin Motors: A Structural Perspective. *Chem Rev* **120**, 5-35 (2020).
879 28. S. Munnich, M. H. Taft, D. J. Manstein, Crystal structure of human myosin 1c--the motor
880 in GLUT4 exocytosis: implications for Ca2+ regulation and 14-3-3 binding. *J Mol Biol* **426**,
881 2070-2081 (2014).
882 29. A. A. Bobkov, E. A. Bobkova, S. H. Lin, E. Reisler, The role of surface loops (residues 204-
883 216 and 627-646) in the motor function of the myosin head. *Proc Natl Acad Sci U S A* **93**,
884 2285-2289 (1996).
885 30. B. H. Varkuti *et al.*, A novel actin binding site of myosin required for effective muscle
886 contraction. *Nat Struct Mol Biol* **19**, 299-306 (2012).
887 31. P. Llinas *et al.*, How actin initiates the motor activity of Myosin. *Dev Cell* **33**, 401-412
888 (2015).
889 32. R. Gong *et al.*, Structural basis for tunable control of actin dynamics by myosin-15 in
890 mechanosensory stereocilia. *Sci Adv* **8**, eabl4733 (2022).
891 33. L. W. Pollard, M. Boczkowska, R. Dominguez, E. M. Ostap, Myosin-1C differentially
892 displaces tropomyosin isoforms altering their inhibition of motility. *J Biol Chem* **300**,
893 107539 (2024).
894 34. A. J. Kee *et al.*, An Actin Filament Population Defined by the Tropomyosin Tpm3.1
895 Regulates Glucose Uptake. *Traffic* **17**, 80-81 (2016).
896 35. C. Veigel *et al.*, The motor protein myosin-I produces its working stroke in two steps.
897 *Nature* **398**, 530-533 (1999).
898 36. S. Pospich, H. L. Sweeney, A. Houdusse, S. Raunser, High-resolution structures of the
899 actomyosin-V complex in three nucleotide states provide insights into the force
900 generation mechanism. *eLife* **10** (2021).

901 37. Q. Lu, J. Li, F. Ye, M. Zhang, Structure of myosin-1c tail bound to calmodulin provides
902 insights into calcium-mediated conformational coupling. *Nat Struct Mol Biol* **22**, 81-88
903 (2015).
904 38. J. Howard, *Mechanics of Motor Proteins and the Cytoskeleton* (Sinauer Associates, Inc.,
905 Sunderland, 2001), pp. 367.
906 39. M. A. Geeves, K. C. Holmes, Structural mechanism of muscle contraction. *Annu Rev*
907 *Biochem* **68**, 687-728 (1999).
908 40. P. D. Coureux, H. L. Sweeney, A. Houdusse, Three myosin V structures delineate
909 essential features of chemo-mechanical transduction. *Embo J* **23**, 4527-4537 (2004).
910 41. I. Rayment *et al.*, Three-dimensional structure of myosin subfragment-1: a molecular
911 motor. *Science* **261**, 50-58 (1993).
912 42. J. Jumper *et al.*, Highly accurate protein structure prediction with AlphaFold. *Nature*
913 **596**, 583-589 (2021).
914 43. D. E. Hokanson, E. M. Ostap, Myo1c binds tightly and specifically to phosphatidylinositol
915 4,5-bisphosphate and inositol 1,4,5-trisphosphate. *Proc Natl Acad Sci U S A* **103**, 3118-
916 3123 (2006).
917 44. D. E. Hokanson, J. M. Laakso, T. Lin, D. Sept, E. M. Ostap, Myo1c Binds Phosphoinositides
918 through a Putative Pleckstrin Homology Domain. *Mol Biol Cell* **17**, 4856-4865 (2006).
919 45. M. Xu *et al.*, Myosin-I Synergizes with Arp2/3 Complex to Enhance Pushing Forces of
920 Branched Actin Networks. *bioRxiv* 10.1101/2024.02.09.579714 (2024).
921 46. F. A. Baez-Cruz, E. M. Ostap, Drosophila class-I myosins that can impact left-right
922 asymmetry have distinct ATPase kinetics. *J Biol Chem* **299**, 104961 (2023).
923 47. T. Lin, M. J. Greenberg, J. R. Moore, E. M. Ostap, A hearing loss-associated myo1c
924 mutation (R156W) decreases the myosin duty ratio and force sensitivity. *Biochemistry*
925 **50**, 1831-1838 (2011).
926 48. J. A. Spudich, S. Watt, The regulation of rabbit skeletal muscle contraction. I.
927 Biochemical studies of the interaction of the tropomyosin-troponin complex with actin
928 and the proteolytic fragments of myosin. *J Biol Chem* **246**, 4866-4871 (1971).
929 49. C. V. Sindelar, K. H. Downing, The beginning of kinesin's force-generating cycle visualized
930 at 9-A resolution. *J Cell Biol* **177**, 377-385 (2007).
931 50. A. Punjani, J. L. Rubinstein, D. J. Fleet, M. A. Brubaker, cryoSPARC: algorithms for rapid
932 unsupervised cryo-EM structure determination. *Nat Methods* **14**, 290-296 (2017).
933 51. S. S. Chavali *et al.*, Cryo-EM structures reveal how phosphate release from Arp3
934 weakens actin filament branches formed by Arp2/3 complex. *Nat Commun* **15**, 2059
935 (2024).
936 52. K. Jamali *et al.*, Automated model building and protein identification in cryo-EM maps.
937 *bioRxiv* 10.1101/2023.05.16.541002 (2023).
938 53. T. I. Croll, ISOLDE: a physically realistic environment for model building into low-
939 resolution electron-density maps. *Acta Crystallogr D Struct Biol* **74**, 519-530 (2018).
940 54. P. Emsley, B. Lohkamp, W. G. Scott, K. Cowtan, Features and development of Coot. *Acta*
941 *Crystallogr D Biol Crystallogr* **66**, 486-501 (2010).
942 55. P. D. Adams *et al.*, PHENIX: a comprehensive Python-based system for macromolecular
943 structure solution. *Acta Crystallogr D Biol Crystallogr* **66**, 213-221 (2010).

56. E. F. Pettersen *et al.*, UCSF ChimeraX: Structure visualization for researchers, educators, and developers. *Protein Sci* **30**, 70-82 (2021).
57. E. C. Meng *et al.*, UCSF ChimeraX: Tools for structure building and analysis. *Protein Sci* **32**, e4792 (2023).